

# **Providing Atomistic Insights of the Dissolution of Rutile Oxides in Electrocatalytic Water-splitting**

## **Supporting Information**

Abhinav S. Raman and Aleksandra Vojvodic\*

*Department of Chemical and Biomolecular Engineering, University of Pennsylvania,  
Philadelphia, PA 19104, USA*

E-mail: [alevoj@seas.upenn.edu](mailto:alevoj@seas.upenn.edu)

# Atomic Models

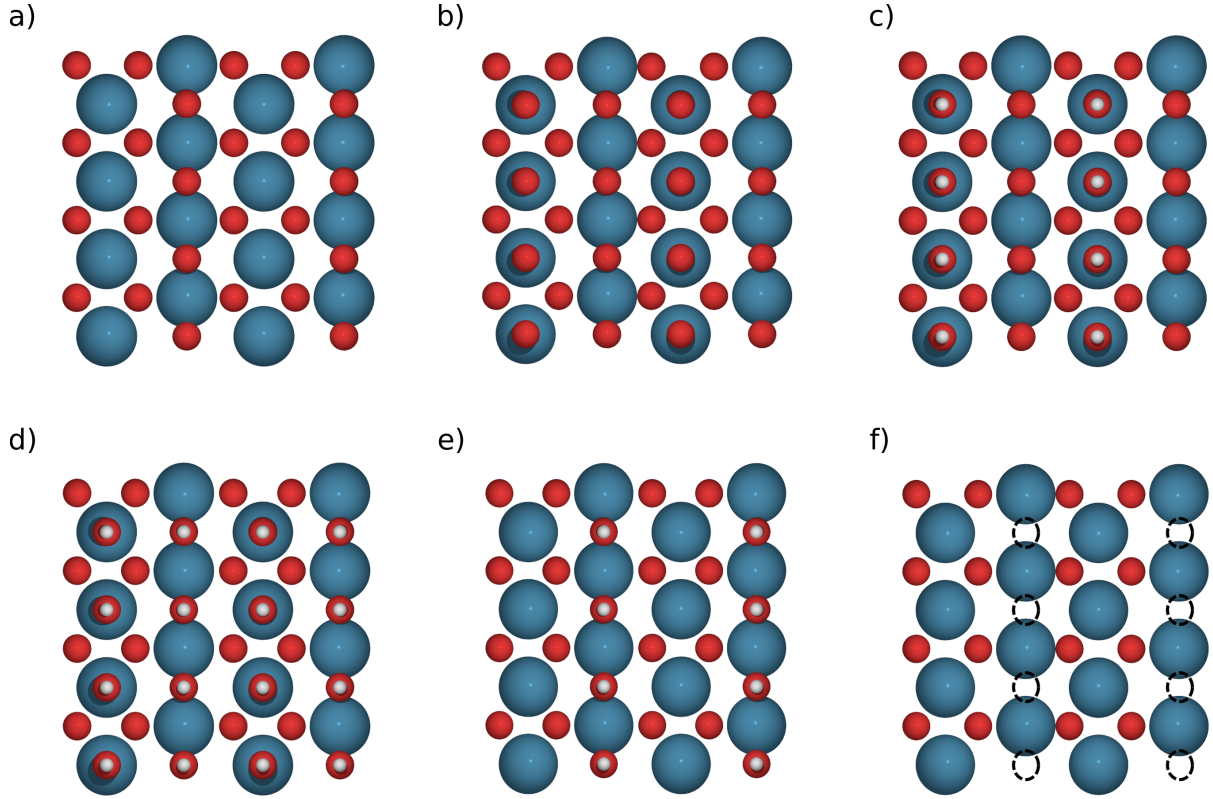


Figure S1: The surface terminations of the (110) facet of the three rutile oxides  $\text{RuO}_2$ ,  $\text{IrO}_2$  and  $\text{TiO}_2$  considered in this study (top-view). a) bulk-cleaved clean surface, b) O adsorbed on the CUS sites c) OH adsorbed on the CUS sites, d) hydroxylated surface (OH adsorbed on CUS and protonated bridge oxygen) e) OH bridge terminated surface and f)  $\text{V}_\text{O}$  bridge terminated surface. Color codes- blue: Ru/Ir/Ti, red: O and white: H.

## Results

### Pourbaix diagram

The preferred terminations in the applied potential range of interest was determined by constructing a Pourbaix diagram using the computational hydrogen electrode approach.<sup>1</sup> The zero-point energy and entropy corrections for O, OH and H were taken from previous studies,<sup>1,2</sup> and the free-energy of the different terminations relative to the bulk-cleaved clean surface was computed as a function of applied potential (U) and pH, as given below:

$$G_{ads} = \Delta G_{ads} - n_e e U_{SHE} - 2.3 n_H k_B T \text{pH} \quad (1)$$

where,  $\Delta G_{ads}$  is the Gibbs free-energy of adsorption,  $n_e$  and  $n_{H^+}$  are the number of electrons and protons respectively,  $U_{SHE}$  is the applied potential relative to the standard hydrogen electrode (SHE),  $k_B$  is the Boltzmann constant, and  $T$  is the temperature. The Pourbaix diagram showing the preferred surface terminations at acidic (pH=1) and alkaline (pH=12) are shown in Figure S2.

After determining the preferred surface terminations as a function of  $U$  and  $pH$ , we systematically created surface vacancies involving the CUS and BR row metals as well as the lattice oxygen they are coordinated with. The different types of vacancies are shown in Figure S3; for the surface termination involving OH adsorbed on the CUS sites.

We then constructed the surface stability (Pourbaix) diagram to determine the thermodynamically favorable surface under oxygen evolution reaction (OER) operating conditions using the ab-initio thermodynamics framework developed in Ref.<sup>3</sup> and applied in Ref.<sup>2</sup> Briefly, the Gibbs free-energy of each surface with the different vacancies was computed relative to the bulk-cleaved clean surface as a function of  $U$  and  $pH$ , as given by:

$$\Delta G = \Delta G_{vac} + \Delta G_{SHE}^0 - n_e e U_{SHE} - 2.3 n_{H^+} k_B T pH + k_B T \ln a_{H_x A O_y z^-} \quad (2)$$

where,  $\Delta G_{vac}$  is the free-energy of vacancy formation obtained from DFT, and the rest of the terms describe the solvation of the atoms leaving the surface described relative to the standard hydrogen electrode (SHE). The Pourbaix diagram showing all the surface vacancies considered for  $IrO_2$ ,  $RuO_2$  and  $TiO_2$  are shown in Figures S4, S5 and S6 respectively. While we have included all of the surface terminations involving different surface vacancies, we note that several surface terminations resulted in large reconstructions, including the desorption of adsorbates, spontaneous formation of  $O_2$  etc. resulting in their relatively lower free-energies. Specifically, these include the 1ML BR-M vacancies in all the three oxides, as well as several others such as the 0.5ML BR-M and BR-MO vacancies in the oxygen terminated (O-CUS-O-BR)  $TiO_2$  surface, and the 1ML CUS-M vacancies in  $TiO_2$ .

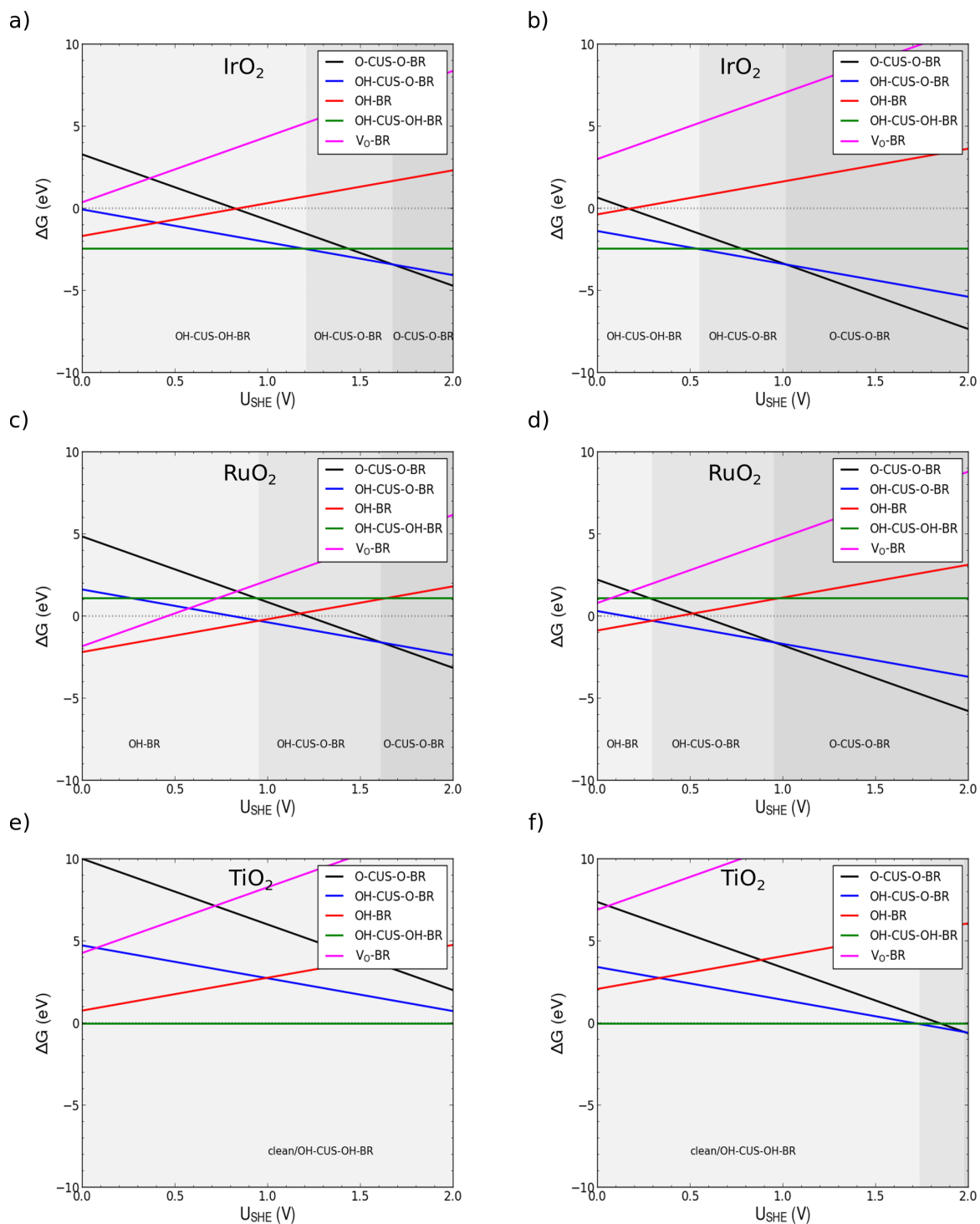


Figure S2: Relative stabilities of the different surface terminations with respect to the bulk-cleaved clean surface as a function of applied potential ( $U$ ) for  $IrO_2$  at a) pH=1 and b) pH=12,  $RuO_2$  at c) pH=1 and d) pH=12, and  $TiO_2$  at e) pH=1 and f) pH=12.

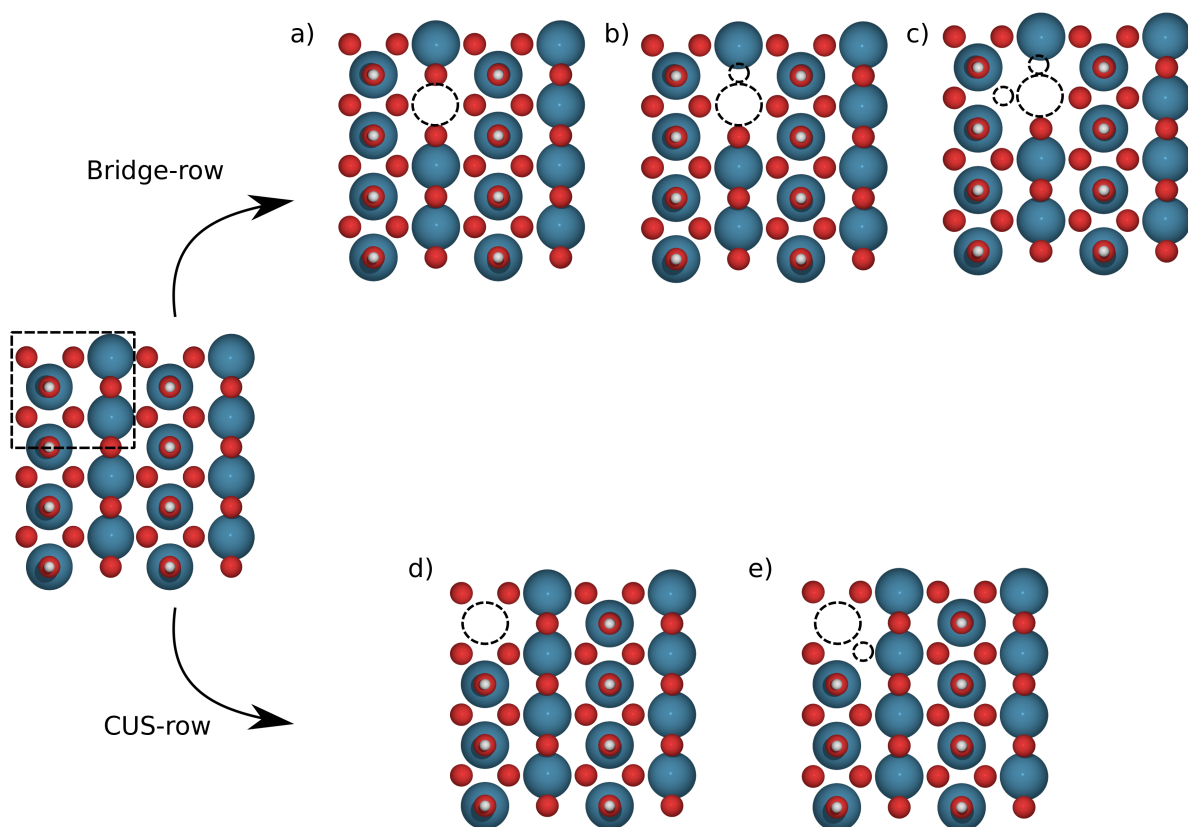
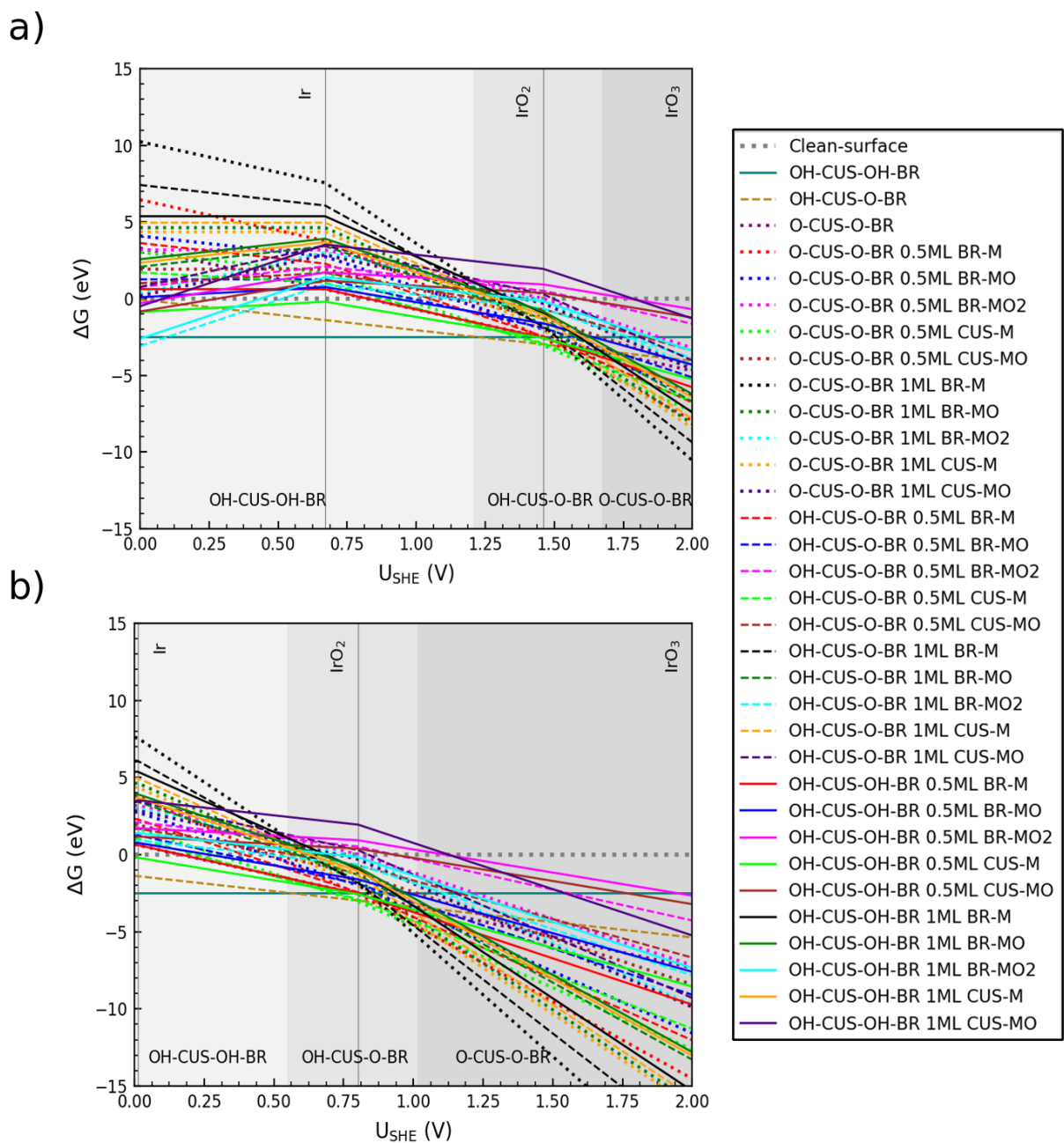
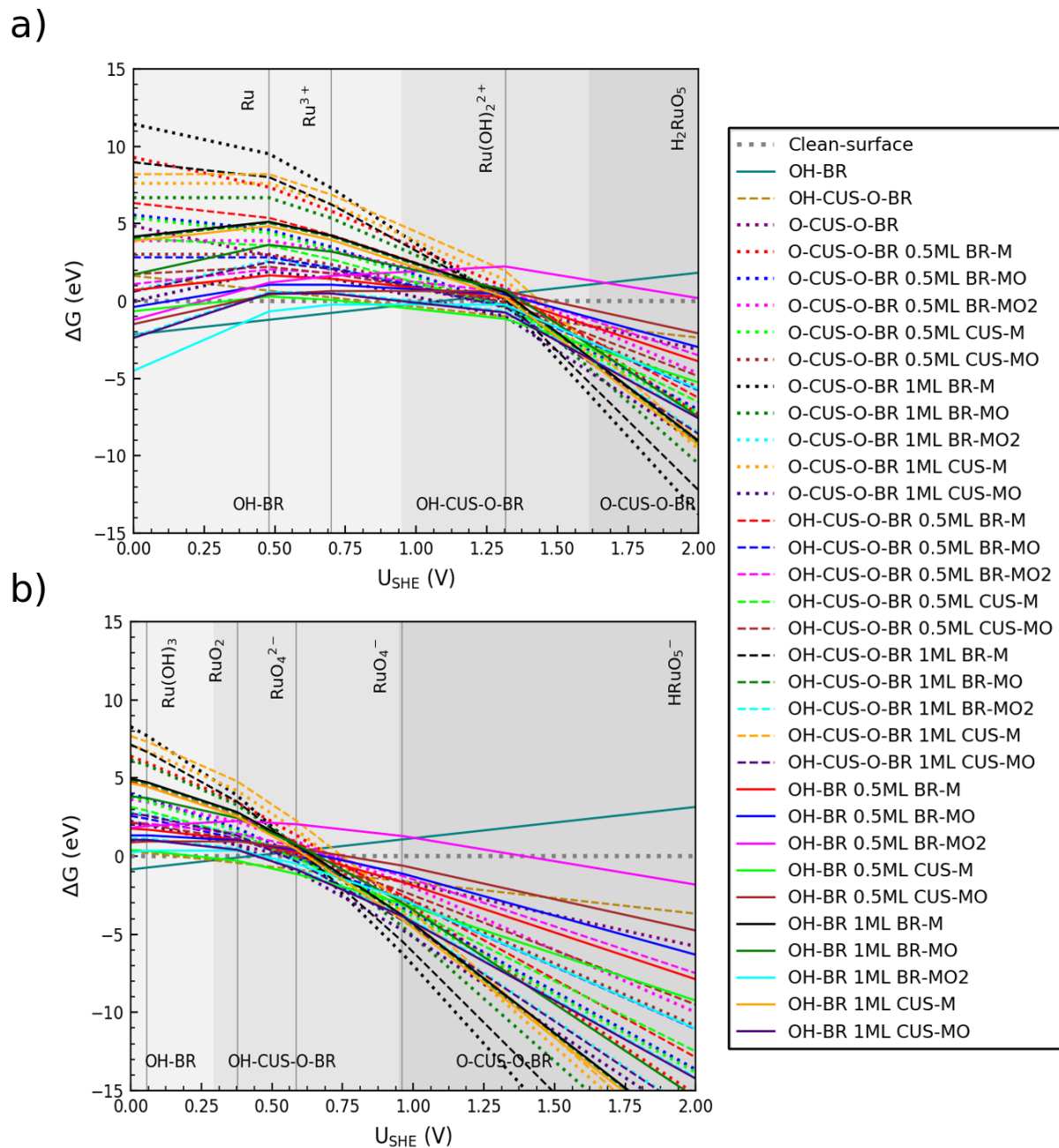


Figure S3: The different types of surface vacancies considered in this study involving the BR and CUS-row metals (top-view); a-c) BR-row surface vacancies; a) BR-M, b) BR-MO and c) BR-MO<sub>2</sub>, and d-e) CUS row surface vacancies; d) CUS-M and e) CUS-MO. Color codes- blue: Ru/Ir/Ti, red: O, white: H, dashed black circles-surface metal and/or oxygen vacancies.





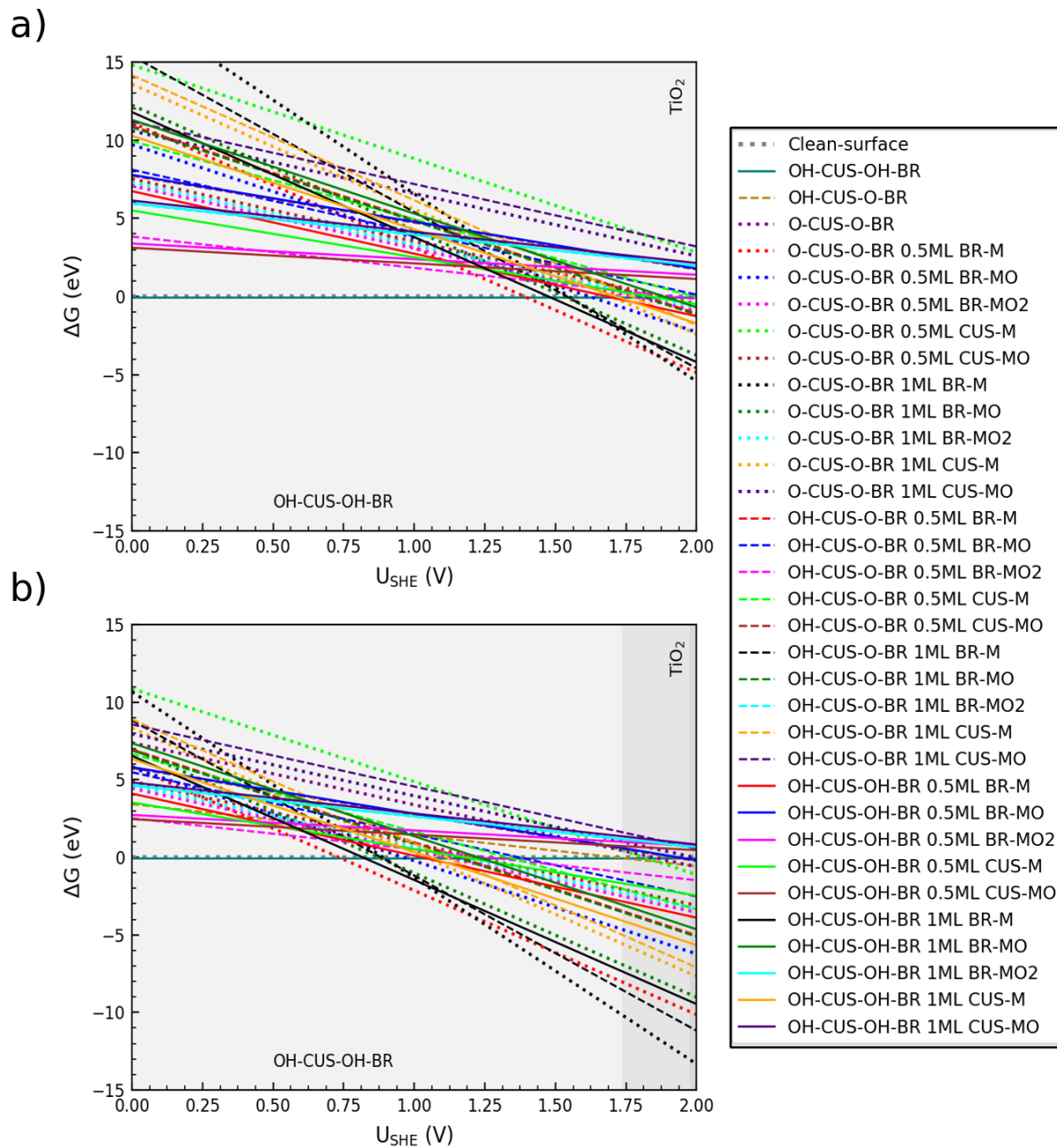


Figure S6: Surface Pourbaix diagram showing the thermodynamically favorable surface terminations of the (110) facet of  $\text{TiO}_2$  at a) pH=1 and b) pH=12 as a function of  $U_{\text{SHE}}$ . The ML vacancy and adsorption coverage are relative to the CUS or BR sites respectively.

## Dissolution paths and Free-energy profiles

For the AISMD and umbrella sampling simulations, the explicit oxide-water interface was constructed as described in the Methods and Models section. Specifically, we considered the differential adsorption energy of adding a water molecule starting from the water-structures corresponding to a 2.5ML surface coverage previously optimized by Siahrostami and Vojvodic.<sup>4</sup> The differential adsorption energy approaching the free energy of a water-molecule in bulk along with the atomic structures of the optimized oxide-water interface are shown in Figure S7.

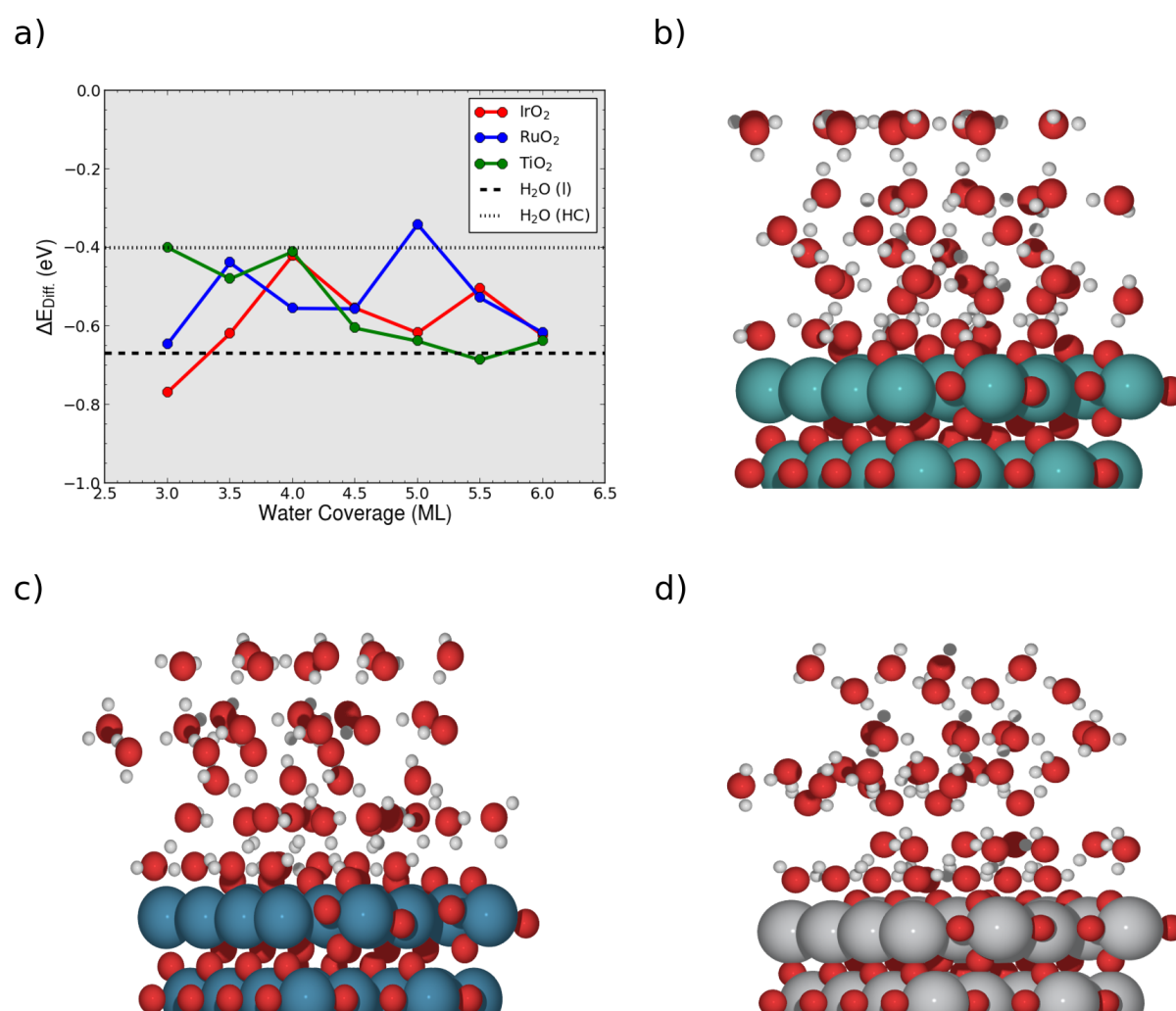


Figure S7: a) Differential adsorption energies for the most stable water structures. The dashed line is the free-energy of a water-molecule in bulk (-0.67 eV) and the dotted line corresponds to the binding energy of one water molecule in the honeycomb (HC) water-structure on the Pt(111) surface (-0.4 eV).<sup>4</sup> Atomic structures (side-view) of the optimized oxide-water interface for b) RuO<sub>2</sub>, c) IrO<sub>2</sub> and d) TiO<sub>2</sub>. Color codes- green: Ru, blue: Ir, grey: Ti, red: O and white: H.

The AISMD scheme is graphically illustrated in Figure S8. Typically we used the distance between the surface metal atom (Ru/Ir/Ti) and the sub-surface oxygen as the only collective-variable to bias. For the dissolution step of  $\text{IrO}_3$  from the (110) rutile  $\text{IrO}_2$  surface, we also considered the metal-oxygen coordination number including the water molecules in the solvent layer closest to the oxide-surface. The coordination number was described by a standard switching-function as defined in PLUMED:<sup>5</sup>

$$S_{ij} = \frac{1 - \left(\frac{r_{ij} - d_0}{r_0}\right)^n}{1 - \left(\frac{r_{ij} - d_0}{r_0}\right)^m} \quad (3)$$

where  $d_0$  is the average bond-length between Ir and O in the oxide taken as  $1.77 \text{ \AA}$ ; and  $r_0$  was fixed to  $0.75 \text{ \AA}$ . We looked at different values for  $n$  and  $m$  as shown in Figure S9, and picked the values of 4 and 10 for  $n$  and  $m$  respectively, that best described the coordination between the Ir and O atoms.

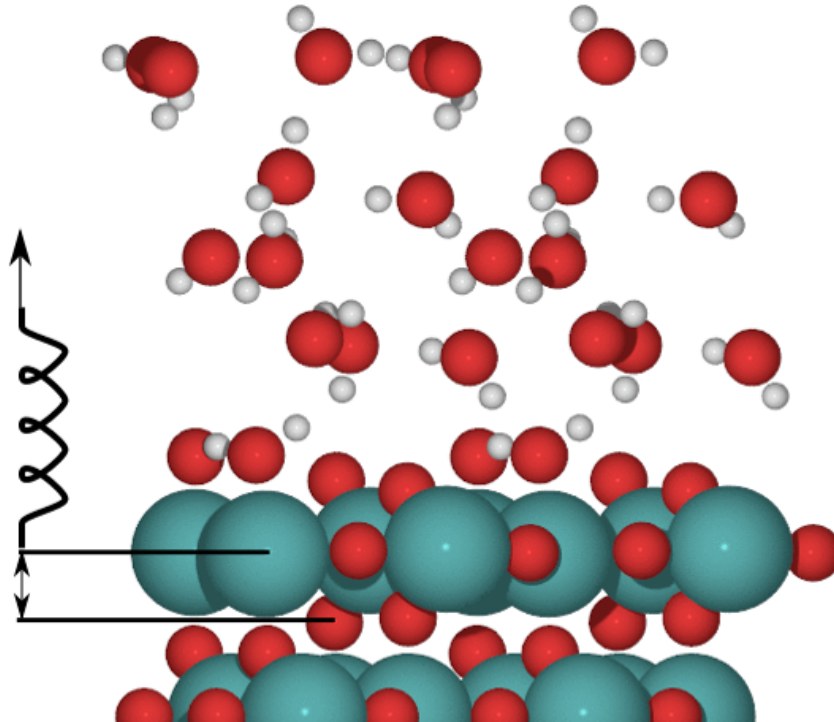


Figure S8: Schematic illustration of the AISMD method employed in this study. Color codes- green: Ru/Ir/Ti, red: O and white: H.

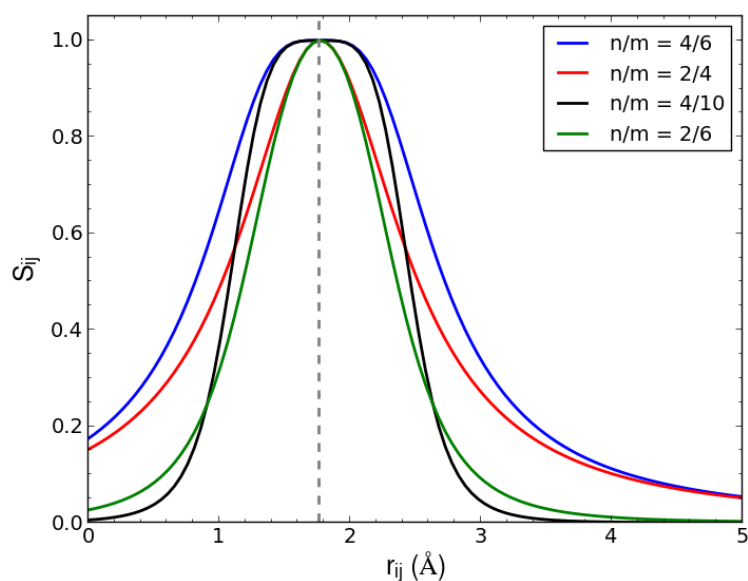


Figure S9: Optimizing the parameters of the switching function used to define the coordination number between Ir and O in  $\text{IrO}_2$ .

The computed free-energy profiles for the different oxides  $\text{IrO}_2$ ,  $\text{TiO}_2$  and  $\text{RuO}_2$  are provided in the Figures below.

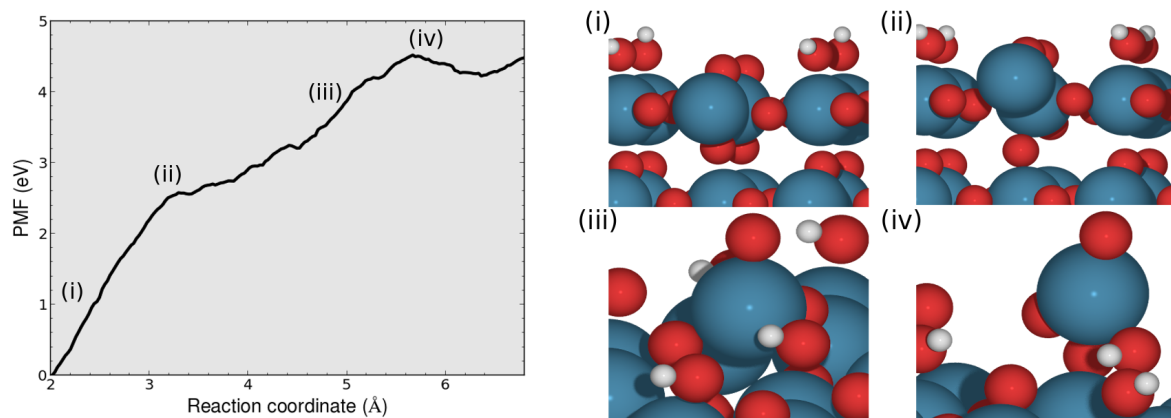


Figure S10: Potential of mean force for the dissolution of Ir from the bridge (BR) site of the (110) surface of  $\text{IrO}_2$ . The corresponding atomic structures of the different configurations along the steered trajectory are shown as inset. Color codes- blue: Ir, red: O and white: H. The solvent molecules have been removed for visualization.

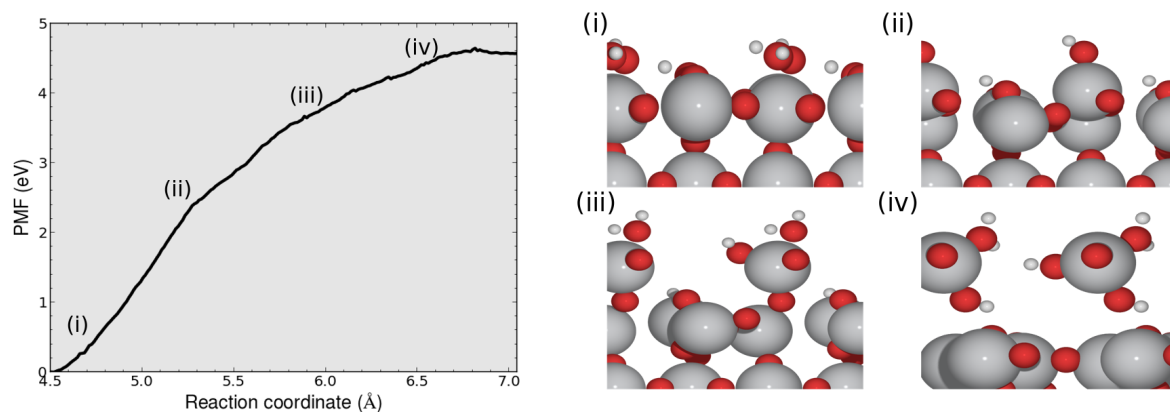


Figure S11: Potential of mean force for the dissolution of Ti from the CUS site of the (110) surface of  $\text{TiO}_2$ . The corresponding atomic structures of the different configurations along the steered trajectory are shown as inset. Color codes- grey: Ti, red: O and white: H. The solvent molecules have been removed for visualization.

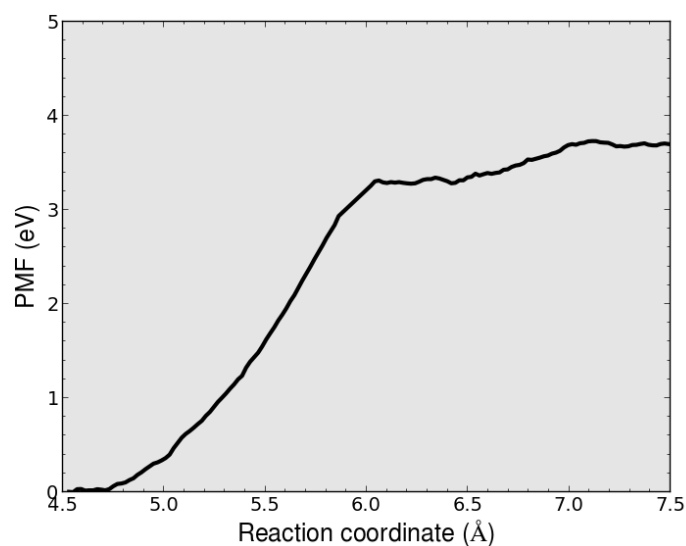


Figure S12: Potential of mean force for the dissolution of Ru from the CUS site of the (110) surface of  $\text{RuO}_2$ , co-dissolving with the Ru from the BR site, shown along the extended reaction coordinate.

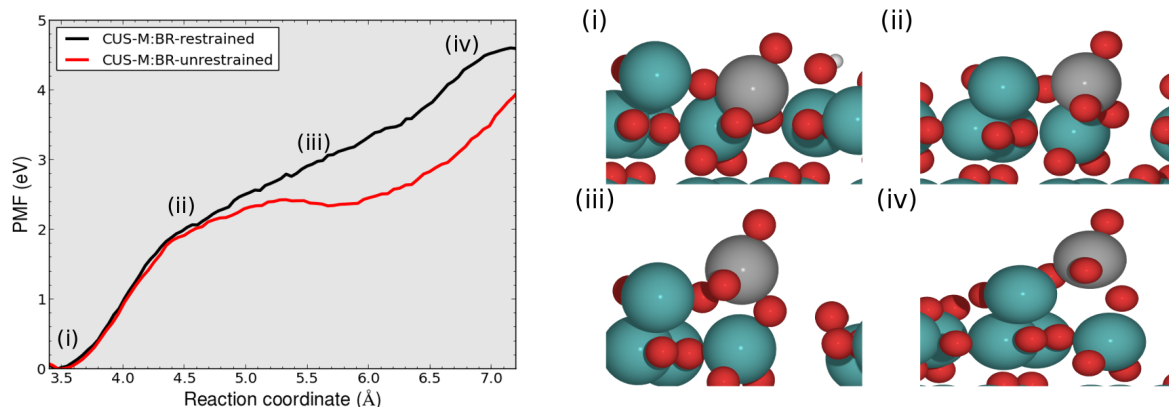


Figure S13: Potential of mean force for the dissolution of the deprotonated Ru from the CUS site of the (110) surface of  $\text{RuO}_2$ , co-dissolving with the Ru from the BR-site. The profiles corresponding to the BR-site with and without applied restraints are shown. The corresponding atomic structures of the different configurations along the steered trajectory are shown as inset. Color codes- grey: dissolving Ru (CUS) atom, green: Ru, red: O and white: H. The solvent molecules have been removed for visualization.

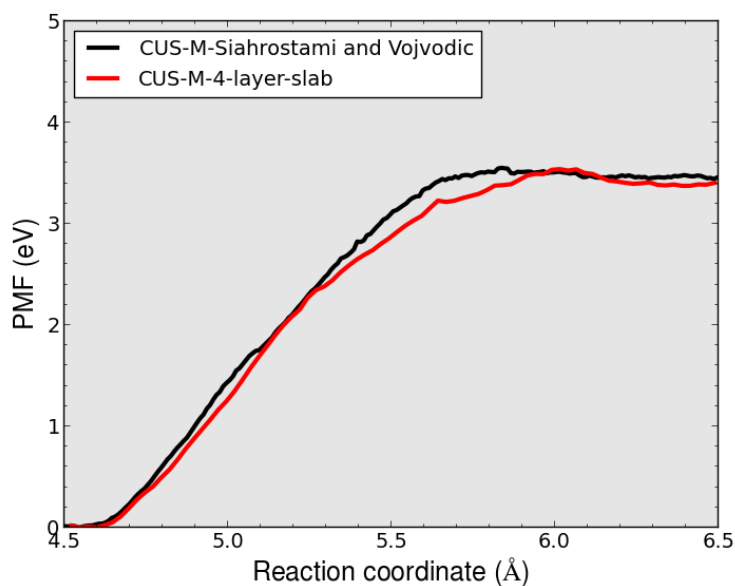


Figure S14: Potential of mean force for the dissolution of Ru from the CUS site of the (110) surface of  $\text{RuO}_2$ , for the slab model taken from Siahrostami and Vojvodic<sup>4</sup> (black) and a thicker 4-layer slab (red); showing the invariance in the calculated PMF with respect to slab thickness

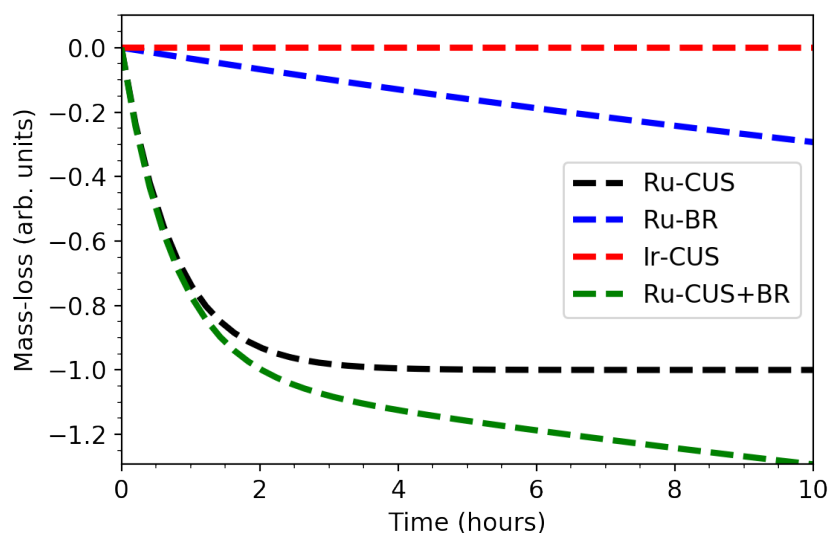


Figure S15: Qualitative estimation of the dissolution rates of the  $\text{RuO}_2$  (110) surface (CUS and BR sites) and  $\text{IrO}_2$  (110) surface (CUS site) expressed as relative mass-loss as a function of time.

The dissolution rates were computed assuming that the process follows first-order kinetics. The rate constant for the dissolution corresponding to each surface site was computed from Transition-state theory (TST) and the calculated potentials of mean force (PMF).<sup>6,7</sup> In order to obtain reasonable rate constants and estimate dissolution rates at time scales compared to experiments, an elevated temperature (1200 K) was employed within the TST approximation.

## References

- (1) Man, I. C.; Su, H. Y.; Calle-Vallejo, F.; Hansen, H. A.; Martínez, J. I.; Inoglu, N. G.; Kitchin, J.; Jaramillo, T. F.; Nørskov, J. K.; Rossmeisl, J. Universality in Oxygen Evolution Electrocatalysis on Oxide Surfaces. *ChemCatChem* **2011**, *3*, 1159–1165.
- (2) Raman, A. S.; Patel, R.; Vojvodic, A. Surface stability of perovskite oxides under OER operating conditions: A first principles approach. *Faraday Discuss.* **2021**, *229*, 75–88.
- (3) Rong, X.; Kolpak, A. M. Ab Initio Approach for Prediction of Oxide Surface Struc-

- ture, Stoichiometry, and Electrocatalytic Activity in Aqueous Solution. *J. Phys. Chem. Lett.* **2015**, *6*, 1785–1789.
- (4) Siahrostami, S.; Vojvodic, A. Influence of Adsorbed Water on the Oxygen Evolution Reaction on Oxides. *J. Phys. Chem. C* **2015**, *119*, 1032–1037.
- (5) Tribello, G. A.; Bonomi, M.; Branduardi, D.; Camilloni, C.; Bussi, G. PLUMED 2: New feathers for an old bird. *Comput. Phys. Commun.* **2014**, *185*, 604–613.
- (6) Chandler, D. Statistical mechanics of isomerization dynamics in liquids and the transition state approximation. *The Journal of Chemical Physics* **1978**, *68*, 2959–2970.
- (7) Carter, E.; Ciccotti, G.; Hynes, J. T.; Kapral, R. Constrained reaction coordinate dynamics for the simulation of rare events. *Chemical Physics Letters* **1989**, *156*, 472–477.